Research Paper

JRSM Cardiovascular Disease
Volume 8: 1–13

DOI: 10.1177/2048004018822428
journals.sagepub.com/home/cvd
SAGE

Estimation of stochastic behaviour in cardiac myocytes: I. Ca^{2+} movements inside the cytosol and sarcoplasmic reticulum on curvilinear domains

Serife Arif, Choi-Hong Lai and Nadarajah I Ramesh

Abstract

Background: Since the discovery of Ca^{2+} sparks and their stochastic behaviour in cardiac myocytes, models have focused on the inclusion of stochasticity in their studies. While most models pay much attention to the stochastic modelling of cytosolic Ca^{2+} concentration the coupling of Ca^{2+} sparks and blinks in a stochastic model has not been explored fully. The cell morphology in in silico studies in the past is assumed to be Cartesian, spherical or cylindrical. The application on curvilinear grids can easily address certain restrictions posed by such grid set up and provide more realistic cell morphology. In this paper, we present a stochastic reaction–diffusion model that couples Ca^{2+} sparks and blinks in realistic shapes of cells in curvilinear domains.

Methodology: Transformation of the model was performed to the curvilinear coordinate system. The set of equations is used to produce Ca^{2+} waves initiated from sparks and blinks. A non-buffered and non-dyed version as well as a buffered and dyed version of these equations were studied in light of observing the dynamics on the two different systems. For comparison, results for both the Cartesian and curvilinear grids are provided.

Results and conclusions: A successful demonstration of the application of curvilinear grids serving as basis for future developments.

Keywords

Stochastic Ca^{2+} waves, Ca^{2+} sparks and blinks, curvilinear domain

Received 24 January 2018; Revised received 6 July 2018; accepted 13 November 2018

Introduction

Ca^{2+}-induced Ca^{2+} release (CICR) is the repeated process in which influx of extracellular Ca^{2+} into the cytosol from L-type channels triggers a release of Ca^{2+} from the sarcoplasmic reticulum (SR) through ryanodine receptors (RyRs) on the z-lines.[1] The CICR process is schematically illustrated in Figure 1. A more detailed review of the processes leading to contraction can be found in Arif et al.[2] The Ca^{2+} release event appears as Ca^{2+} sparks[3–8] in the cytosol and Ca^{2+} blinks[9] in the SR. The successive activation of RyRs increases the local Ca^{2+} concentration in the cytosol. This process is called Ca^{2+} transient.[10–12] Ca^{2+} sparks observed in the heart muscle were found to behave stochastically[4] and that release occurs at discrete sites closely associated with transverse (t)-tubules at Z-lines[13] with regular spacing of 1.8–1.9 μm longitudinally and more irregularly with a mean value of 0.79 μm transversely.[8]

In cardiac ventricle cells, spontaneous propagating waves of Ca^{2+} may occur due to Ca^{2+} overload which is believed to occur under pathological conditions. This can affect the heart's normal function and may lead to ventricular arrhythmias and heart failure.[14,15] Therefore, it has become increasingly important to

Department of Mathematical Sciences, Faculty of Architecture, Computing and Humanities University of Greenwich, London, UK

Corresponding author:
Serife Arif, Department of Mathematical Sciences, Faculty of Architecture, Computing and Humanities University of Greenwich, London, UK.
Email: s.arif@greenwich.ac.uk

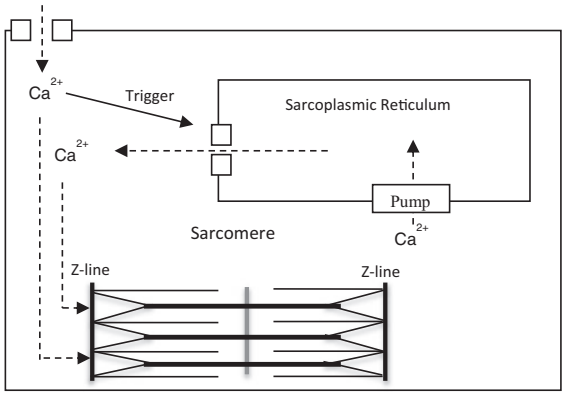

Figure 1. Schematic view of the influx and efflux of Ca^{2+} in a cardiac myocyte. Ca^{2+} entry through L-type channels on the sarcolemma triggers Ca^{2+} release from the SR. This is a repeated process of the CICR mechanism. The Ca^{2+} released from the SR increases the concentration in the cytosol. Ca^{2+} here travels to the sarcomeres and interacts with filaments and activates the contractile machinery. Upon relaxation, Ca^{2+} disassociates from the filaments and is pumped back into the SR by the SERCA pumps. Modified from Arif et al.[2]

understand the underlying mechanism of the CICR process and any experimental or mathematical studies would contribute towards this.

Several models have been used to simulate the Ca^{2+} sparks and waves. A number of them are partially based on the CICR process and the release from RyRs is described as either deterministic[16–26] or stochastic.[15,27–30] The models mainly consist of fractional differential equations (FDEs), partial differential equations (PDEs), and ordinary differential equations (ODEs). Although some of these models include buffers and dye and others do not, they all shape our understanding of the underlying mechanism of CICR in cardiac myocytes. Throughout the years models have been refined to account for more buffers and a more realistic representation of the calcium release units (CRUs).

Backx et al. described the CICR process with magnesium buffer reactions using a one-dimensional model that only takes into account longitudinal diffusion.[16] The Ca^{2+} release from the SR occurs at CRUs and is assumed to be a time dependent process with an exponential rise and fall of the Ca^{2+} flux from the SR. The occurrence was dependent on a threshold for Ca^{2+} concentration which leads to a deterministic description of this term in the model. A similar deterministic formulation was incorporated in the release flux by Soeller and Cannell which was then included in the total calcium current by volume integration.[17] The aim was to experimentally test the extraction of the release flux underlying calcium sparks including a more detailed dye and buffer binding structure.

Another deterministic construction of the SR calcium release was represented in two-dimensional models[21–23] so the spatial and anisotropic properties of the cytosolic Ca^{2+} diffusion can be successfully reproduced. In these models, the diffusion of Ca^{2+} sparks obeys Fick's Law. Later on, an anomalous subdiffusion model was proposed based on an FDE that represents the cytosolic Ca^{2+} concentration[24,26] and it was shown to reproduce the spatial characteristic of sparks more realistically.

There have also been deterministic models with no buffer reactions.[18–20] These models focused on representing the CICR process in a compartmental model with no dye and buffer reactions. No virtual point sources of CRUs are described. Instead the SR Ca^{2+} release is associated with a nonlinear term based on the cytosolic and sarcoplasmic concentrations applied to all spatial points of the computational domain. In 2009, this two-pool CICR model was integrated into a force-calcium relation by Tracqui and Ohayon to successfully reproduce Ca^{2+} waves and the resulting phases of contraction using cylindrical coordinates.[25]

More recently, stochasticity is introduced into models[27] in which the Ca^{2+} channel opening depends on a probability function. Lu et al. integrated rogue RyRs into this model to simulate the effect of these receptors on the Ca^{2+} wave in ventricular myocytes with heart failure.[15] These models were extended from Fick's Law-based Ca^{2+} diffusion to anomalous subdiffusion.[28,29] This has greatly improved our understanding of the calcium dynamics under pathological conditions. The majority of stochastic models focus on the coupling of cytosolic and sarcoplasmic Ca^{2+} concentrations using only one equation to represent this coupled state. This equation is usually used to track the change of cytosolic Ca^{2+} concentration in space and time. In order to measure or observe the change in sarcoplasmic Ca^{2+} concentration a separate equation is required for this which is yet to be fully explored under stochastic conditions. One recent work by Li et al.[30] is based on two governing equations. One is based on anomalous subdiffusion that models the Ca^{2+} sparks and waves in the cytosol and the other models the Ca^{2+} blinks in the SR. One limitation to this work is the use of a Cartesian domain in representing the cell structure which can cause difficulty in modelling Ca^{2+} waves in more complicated cell shapes.

The main motivation of this work concerns the cell domain considered in the computational studies. The majority of models to date, focus on representing the cell morphology using simplified domains applied to Cartesian, spherical[17] or cylindrical coordinates.[31] However, these can become impractical for more complicated shaped cells. Using a simplified domain to represent such complicated shapes can be useful, however,

insufficient for the accurate estimation especially at the boundaries. An alternative method that can address this problem is the use of finite element method (FEM) which has been implemented before for the modelling of contraction in isolated cardiac myocytes.[25,32] In this work, an alternating direction implicit (ADI) method with curvilinear coordinate transformation technique is used. ADI is a finite difference-based method and is more computationally efficient than FEM and the method itself is also easier to implement. Finite difference-based methods are a good alternative to FEM, however, it has not been used in this area in combination with a curvilinear transformation technique. This is the first work to have ever used a finite difference-based method with a curvilinear coordinate transformation technique for estimating stochastic Ca^{2+} movement in a cardiac myocyte with and without buffers and dye.

The aims of the present paper are (1) extension of the stochastic formulation by Izu et al.[27] to include the Ca^{2+} sparks coupled with Ca^{2+} blinks and its application on curvilinear domains (this allows one to work on real cell morphology); (2) representation of two different systems: (a) buffered and dyed system to account for Ca^{2+} movement observed in in vitro studies and (b) non-buffered and non-dyed system to observe the difference between the two systems; (3) comparison of the Cartesian and curvilinear domains. The model and its extension to curvilinear grids are described in the next section. The application to curvilinear grids and comparison results between models are presented in the results section with conclusions and potential future improvements discussed in the final section of this paper.

Methods

Mathematical model for Ca^{2+} sparks and Ca^{2+} blinks with buffer and dye

The set of differential equations (DEs) by Izu et al.[22,23,27] describing the cytosolic Ca^{2+} concentration with buffer and dye binding properties is modified to include an additional term for the cytosolic leak[19,20,25] and a slightly different representation of the SR leak term.[19,20,25] An extension to this model here includes a coupling of the cytosolic Ca^{2+} diffusion with the sarcoplasmic Ca^{2+} concentration. For simplicity, diffusion is restricted to follow Fick's Law and the Ca^{2+} concentration in the SR is restricted to time diffusion and so is not diffusive in space giving rise to a simple ODE. This is adopted from several other authors[18–20,25,32,33] and was shown to produce promising results. Therefore, for the current study it will suffice to use these assumptions for computational simplicity. Considering the above, the reaction–diffusion equations are expressed as

$$\frac{\partial C_{cyt}}{\partial t} = D_{Cx}\frac{\partial^2 C_{cyt}}{\partial x^2} + D_{Cy}\frac{\partial^2 C_{cyt}}{\partial y^2} + J_{dye} + J_{buffer} - J_{pump} - J_{Ca^{2+}\,leak} + J_{CRU} - J_{SR\ \ leak} \tag{1}$$

$$\frac{\partial C_{SR}}{\partial t} = J_{SR\,leak} + J_{pump} - J_{CRU} + J_{dye} + J_{buffer} \tag{2}$$

$$\frac{\partial [CaF]}{\partial t} = D_{Dx}\frac{\partial^2 [CaF]}{\partial x^2} + D_{Dy}\frac{\partial^2 [CaF]}{\partial y^2} - J_{dye} \tag{3}$$

$$\frac{\partial [CaB]}{\partial t} = -J_{buffer} \tag{4}$$

where $C_{cyt} = [Ca^{2+}]_{cyt}$ is the free Ca^{2+} concentration in the cytosol; $C_{SR} = [Ca^{2+}]_{SR}$ is the free Ca^{2+} concentration in the SR; $[CaF]$ and $[CaB]$ are the concentrations of Ca^{2+} bound dye and buffer; D_{Cx} and D_{Cy} are cytosolic Ca^{2+} diffusion coefficients in the longitudinal and transverse directions; D_{Dx} and D_{Dy} are diffusion coefficients of the Ca^{2+} bound dye in the longitudinal and transverse directions, respectively. Ca^{2+} diffusion is reported to be anisotropic[34] with diffusion twice as fast along the sarcomere orientation than that in the transverse direction.[31] Standard values used satisfy experimental data that $\frac{D_{Cy}}{D_{Cx}} = 0.5$ and are given in Table 1 along with a short description. Fluxes due to Ca^{2+} fluorescent indicator dye, J_{dye}, and endogenous stationary buffers, J_{buffer}, are

$$J_{dye} = -k_F^+ C_{cyt}\left([F]_T - [CaF]\right) + k_F^-[CaF]$$

$$J_{buffer} = -k_B^+ C_{cyt}\left([B]_T - [CaB]\right) + k_B^-[CaB]$$

k_j^+ and k_j^- are forward and reverse rate constants for dye ($j = F$) and buffer ($j = B$); $[F]_T$ and $[B]_T$ are total concentration of the indicator dye and buffers, values of which are given in Table 1. J_{pump}, $J_{Ca^{2+}\ leak}$, $J_{SR\ leak}$ represent the pumping rate of SR Ca^{2+}-ATPase, Ca^{2+} leak from the cytosol and SR, respectively. The formulation of these terms are adopted from work by several others in the field[18–20,25,32,33] and shown to produce promising results. These terms are given as

$$J_{pump} = V_{pump}\frac{C_{cyt}^{npump}}{K_{pump}^{n_{pump}} + C_{cyt}^{n_{pump}}}$$

$$J_{Ca^{2+}\ \ leak} = kC_{cyt}$$

Table 1. Standard parameter values.[22,23,27–29]

Parameter	Value	Units	Notes
D_{Cx}, D_{Cy}	0.3, 0.15	$\mu m^2/ms$	Ca^{2+} diffusion coefficients
D_{Dx}, D_{Dy}	0.02, 0.01	$\mu m^2/ms$	Diffusion coefficients of dye
l_x, l_y	2, 0.8	μm	Spacing of CRUs in x and y
$[Ca^{2+}]_{cyt(\infty)}$	0.1	μM	Initial Ca^{2+} concentration
F	96500	C mol^{-1}	Faraday's constant
V_{pump}	0.208	$\mu M/ms$	Maximum SR pump rate
K_{pump}	0.184	μM	SR pump Michaelis constant
K_{prob}	15	μM	Ca^{2+} sensitivity parameter
n_{pump}, n_{prob}	3.9, 1.6	–	Hill coefficients
T_{open}	10	ms	Duration of current flow through CRU
P_{max}	0.3	per CRU ms^{-1}	Maximum probability of Ca^{2+} spark occurrence
σ_3	$I_{CRU}/2F$	mole/ms	Three-dimensional Ca^{2+} source strength
k_f^+, k_B^+	80, 100	$(\mu Ms)^{-1}$	Forward rate constants for dye and buffer reactions
k_f^-, k_B^-	90, 100	s^{-1}	Reverse rate constants for dye and buffer reactions
$[F]_T$, $[B]_T$	50, 123	μM	Total concentration (bound + unbound) of fluorescent dye and buffer

CRUs: calcium release units; SR: sarcoplasmic reticulum.

$$J_{SR\ leak} = k_f C_{SR}$$

in which V_{pump}, K_{pump} and n_{pump} represent the maximal rate, affinity constant and the Hill exponent for Ca^{2+} uptake into SR, while k and k_f are constants for Ca^{2+} efflux from cytosol to extracellular medium and from SR into cytosol, respectively.

The SR Ca^{2+} release term, J_{CRU}, is used by several others including Lu et al.[15], Izu et al.[27] and Chen et al.[28,29] where the cytosolic Ca^{2+} wave propagation initiated from either the boundary of center was successfully reproduced and the statistics and properties were studied and compared against experimental properties or snapshots. This term is expressed as

$$J_{CRU} = \sigma \sum_{i,j} \delta(x - x_i)\delta(y - y_j)S(x_i, y_j, t; T_{open}), \quad \sigma = K_s\sigma_3$$

Molar flux through the RyRs, σ, is associated with the source strength, K_S, and the three-dimensional source strength, $\sigma_3 = I_{CRU}/2F$. K_s needs to be derived for a two-dimensional model (see equation (7) in Appendix 1).

The CRUs are placed at regular intervals of l_x along the x-axis and l_y along the y-axis. It is assumed that once a CRU opens it will remain open for 10 ms (i.e. $T_{open} = 10$) after which it will switch to a closed state and will not reopen (a long refractory period). An adjustment to the source strength was previously done to approximate the molar flux of a point source.[23] This approach is adopted here for a general two-dimensional case[35] (see Appendix 1 for the obtained σ values for the two-dimensional case). The locations of the CRUs are identified through the Dirac delta function, δ where there is a channel (i.e. $x - x_i = 0$ implies that $\delta = 1$ which denotes there is a channel otherwise $x - x_i \neq 0$ indicates no channel $\delta = 0$). The stochastic term, S, controls the firing of the CRU when a probability condition is satisfied

$$S(x_i, y_j, t; T_{open}) = \begin{cases} 1, & \dfrac{P}{P_{max}} > u \\ 0, & \dfrac{P}{P_{max}} \leq u \end{cases}$$

where $P(C(x, y, t), K_{prob}, n_{prob}) = P_{max}C_{cyt}^{n_{prob}}/(K_{prob}^{n_{prob}} + C_{cyt}^{n_{prob}})$, P_{max} is the maximum probability of Ca^{2+} spark occurrence, K_{prob} represents the Ca^{2+} sensitivity factor and n_{prob} is the Hill coefficient. At each time step, Δt, a uniformly distributed random number, u, is generated and compared to the probability function P calculated from the Ca^{2+} concentration. A CRU fires if $P/P_{max} > u$ and thus $S = 1$ otherwise (i.e. in the case where $\frac{P}{P_{max}} < u$) a CRU will remain closed, i.e. $S = 0$.

Cartesian and curvilinear domains

The computational domain for the cell is represented by two different coordinate systems, namely Cartesian and curvilinear. It is assumed that the SR spans the size of the respective computational domains used. Two different systems are solved on the Cartesian and curvilinear domains: (1) non-buffered and non-dyed (NBND) system (i.e. $J_{dye} = J_{buffer} = 0$) and (2) buffered and dyed (BD) system. Certain parameter values such as the initial SR Ca^{2+} concentration (i.e. $[Ca^{2+}]_{SR(\infty)}$), k, k_f, and I_{CRU} required modification when moving from an NBND system to a BD system in order to

achieve a strong propagation of Ca^{2+} wave. These parameter values are given in Table 2.

A two-dimensional domain is considered with the Cartesian and curvilinear grids shown in Figure 2. The Cartesian problem (Figure 2, top) is solved with equations (1) to (4). Finite discretisation of the PDEs is used and an ADI method[36] is used as the numerical scheme. The ODE for the sarcoplasmic Ca^{2+} concentration is solved by using a fourth order Adams-Bashforth (AB) method and the other ODEs are solved by using the traditional forward Euler method.

Table 2. Parameter values for NBND and BD cases applied to the Cartesian and curvilinear grids.

	NBND		BD		
Parameter	Cartesian/ curvilinear	Source	Cartesian/ curvilinear	Source	Units
$[Ca^{2+}]_{SR(\infty)}$	750		1000	30	μM
k	2	25	2.5	19,25	s^{-1}
k_f	0.2	25	0.25	19,25	s^{-1}
I_{CRU}	6		30		pA

Note: Some values used in the case of the BD system are within the range of the cited values.
NBND: non-buffered and non-dyed; BD: buffered and dyed.

In the curvilinear case, the diffusion equations (1) and (3) need to be transformed from the Cartesian-based system with the gridlines specified by x and y to the curvilinear coordinate system with gridlines specified by ξ and η prior to discretisation. Transforming equations (1) and (3) leads to

$$\begin{aligned}\frac{\partial C_{cyt}}{\partial t} = &\left(D_{Cx}\left(\frac{\partial \xi}{\partial x}\right)^2 + D_{Cy}\left(\frac{\partial \xi}{\partial y}\right)^2\right)\frac{\partial^2 C_{cyt}}{\partial \xi^2} \\ &+ 2\left(D_{Cx}\frac{\partial \xi}{\partial x}\frac{\partial \eta}{\partial x} + D_{Cy}\frac{\partial \xi}{\partial y}\frac{\partial \eta}{\partial y}\right)\frac{\partial^2 C_{cyt}}{\partial \xi \partial \eta} \\ &+ \left(D_{Cx}\left(\frac{\partial \eta}{\partial x}\right)^2 + D_{Cy}\left(\frac{\partial \eta}{\partial y}\right)^2\right)\frac{\partial^2 C_{cyt}}{\partial \eta^2} + J_{dye} \\ &+ J_{buffer} - J_{pump} - J_{Ca^{2+}\,leak} + J_{CRU} - J_{SR\,leak}\end{aligned} \tag{5}$$

$$\begin{aligned}\frac{\partial [CaF]}{\partial t} = &\left(D_{Dx}\left(\frac{\partial \xi}{\partial x}\right)^2 + D_{Dy}\left(\frac{\partial \xi}{\partial y}\right)^2\right)\frac{\partial^2 [CaF]}{\partial \xi^2} \\ &+ 2\left(D_{Dx}\frac{\partial \xi}{\partial x}\frac{\partial \eta}{\partial x} + D_{Dy}\frac{\partial \xi}{\partial y}\frac{\partial \eta}{\partial y}\right)\frac{\partial^2 [CaF]}{\partial \xi \partial \eta} \\ &+ \left(D_{Dx}\left(\frac{\partial \eta}{\partial x}\right)^2 + D_{Dy}\left(\frac{\partial \eta}{\partial y}\right)^2\right)\frac{\partial^2 [CaF]}{\partial \eta^2} - J_{dye}\end{aligned} \tag{6}$$

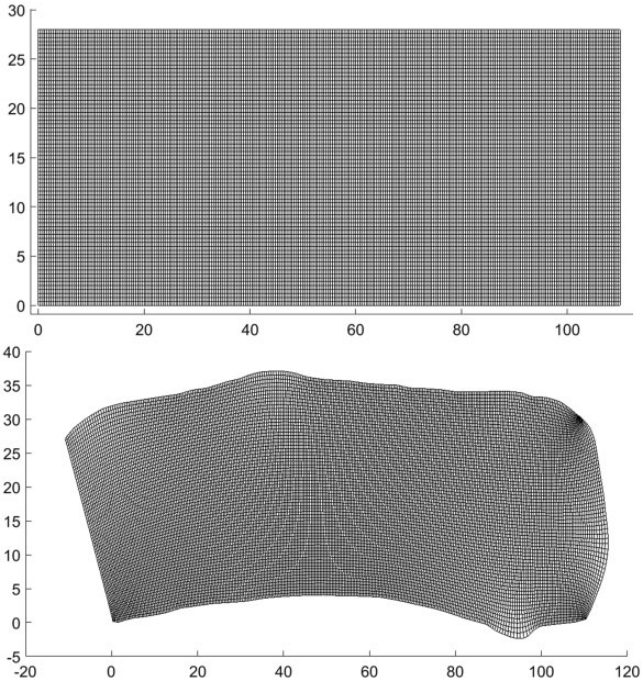

Figure 2. Grids generated on the Cartesian (top) and curvilinear (bottom) coordinate system. In both cases, the system is discretised into 276×71 grid points. A cell size of 110 μm length and 28 μm width is considered. Data for the generation of curvilinear coordinates are extracted from successive snapshots of a real cell morphology provided by Tracqui and Ohayon at time t_4.[25] The CRDT algorithm used in the generation of the curvilinear coordinates ensures the smooth distribution of the grid points throughout the curvilinear domain.

These equations are then solved by using the ADI method.[36] The source strength becomes spatially dependent since the distance between grid points is not uniform. Equations (2) and (4) to (6) are then solved on the curvilinear grid (Figure 2, bottom).

Orthogonal curvilinear coordinates are generated using the software gridgen-c developed by Sakov and CSIRO Marine Research (2006–2017) (see acknowledgement). The code incorporates a CRDT algorithm by Driscoll and Vavasis for conformal mapping[37] which smoothly distributes the grid points throughout the domain. This algorithm provides the x and y positions of the curvilinear grid which is then used along with a 10th order compact finite difference scheme[38] to evaluate the derivatives associated with the curvilinear coordinates $\partial\xi/\partial x$, $\partial\xi/\partial y$, $\partial\eta/\partial x$ and $\partial\eta/\partial y$ in equations (5) and (6).

The CRUs are distributed with $l_x = 2$ μm spacing in the longitudinal and $l_y = 0.8$ μm spacing in the transverse directions. In the curvilinear case, the number of spacing between CRUs is determined by setting equal number of grid points between channels leading to a pointwise evenly spread channels in both directions. The distribution of these channels is given on both Cartesian and curvilinear grids in Figure 3.

As boundary conditions zero-flux is assumed at the cell boundaries by imposing $\partial C_{cyt}/\partial x = \partial C_{cyt}/\partial y = 0$. Similar assumption is imposed on the equation for the Ca^{2+} bound dye, i.e. $\partial[CaF]/\partial x = \partial[CaF]/\partial y = 0$. These conditions are widely used in previous works[16,21–23,27–29] and shown to provide good results.

In the next section of this paper, temporal concentration profiles are provided for the cytosolic and sarcoplasmic Ca^{2+} concentrations. Sensors are placed in both domains to record these concentration values. The exact location of these sensors is given in Figure 3. In addition to these results, the mean wave velocity of Ca^{2+} propagation is provided in each case. For the estimation of the velocity, the peak of the Ca^{2+} wave is tracked from a point close to the centre to the end of either side of the domain. The distance travelled (in μm) is then divided by the time (in seconds) taken to reach the end. An average is taken from five simulations to provide a mean velocity value.

Results

In cardiac myocytes, Ca^{2+} waves propagate as sharp bands[39] with velocities and frequencies that are high enough to allow for the simultaneous propagation of distinct fronts in a given individual cell. The latter type of wave has been called type 1 for convenience.[33]

In the following results, Ca^{2+} waves of type 1 is observed. Once sparks are initiated they develop in 10 ms and increase the concentration around the region. The probability of firing is proportionally dependent on the local concentration. Therefore, a rise in concentration increases the probability of SR release and eventually leading to the activation of neighbouring CRUs. If the concentration is sufficiently high more CRUs fire consecutively which creates a propagating Ca^{2+} wave.

In all cases that are presented in this section, the initial cytosolic Ca^{2+} concentration at rest is set to $[Ca^{2+}]_{cyt(\infty)} = 0.1$ μM. The concentration in the SR compartment is 500–1000 μM and is 2–3 orders of

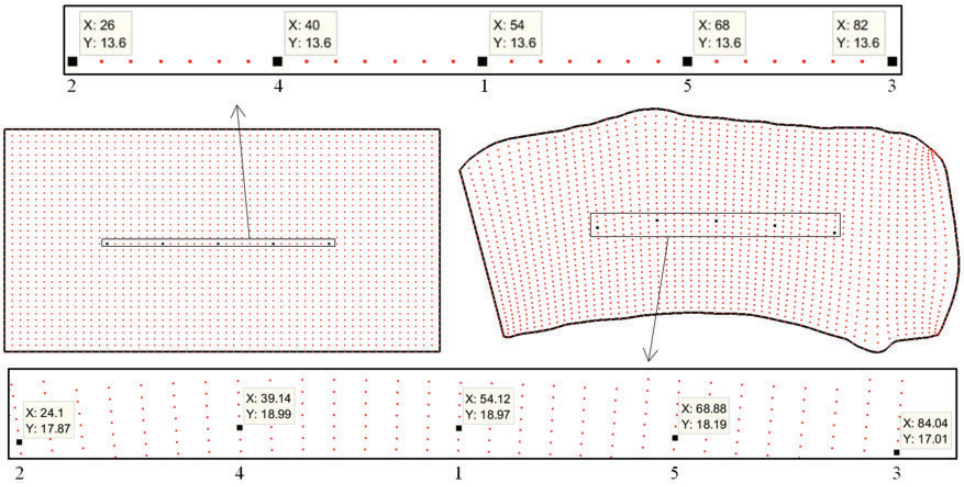

Figure 3. Distribution of the CRU channels on the Cartesian (left) and curvilinear (right) domains. The CRUs are uniformly distributed in the Cartesian case while in the curvilinear case, they are spaced out evenly with an equal number of grid points between them leading to the distribution to appear denser at the concave (top bending) and coarser at the convex (bottom bending) regions. Sensors are also included in the domains with their x and y coordinates in μm and their sensor number below. The locations of the sensors are marked as black squares.

magnitude greater than that in the cytosol. Therefore, in the simulations presented here the initial concentration in the SR is set to 750 μM in the NBND system and 1000 μM in the BD systems. Simulations begin with 5×4 CRUs force activated in the middle of the domain in order to set off initial sparks. The temporal grids are set up with time step size of $\Delta t = 0.1$. The spatial step sizes in the Cartesian case are set to $\Delta x = \Delta y = 0.4$ and that in the curvilinear case is spatially dependent so will vary throughout the domain.

NBND system on the Cartesian and curvilinear domains

In this section, results are presented for the NBND system. The set of equations (1) to (4) are solved on the Cartesian domain and equations (2) and (4) to (6) on the curvilinear domain. Buffer and dye reactions are neglected in the model, i.e. $J_{dye} = J_{buffer} = 0$, in order to distinguish the effects of such reactions on the wave propagation velocity and amplitude. Solving the NBND system on both the Cartesian and curvilinear domains with the CRU distribution given in Figure 3, we obtain the results in Figures 4 (Cartesian) and 5 (curvilinear). Images show the development of the initial sparks in 10 ms and its propagation towards and along the boundaries at the top and bottom until it reaches and propagates outwards from the boundaries at the ends (left and right).

Looking at the simulation time when the Ca^{2+} reaches the end boundaries it was observed that the wave propagates in less time compared to that in the curvilinear case. As can be seen in Figure 6, the peak of the wave exits the domain in 200 ms in the Cartesian (Figure 6(a)) and 400 ms in the curvilinear (Figure 6(b)) cases. The longitudinal mean velocity of the wave is calculated to be approximately 312.41 μm/s with amplitudes approximately ranging 17–20.04 μM in the Cartesian (Figure 7(a)) and 180.98 μm/s with amplitudes approximately ranging 19.23–23.79 μM in the curvilinear cases (Figure 7(c)).

There is a periodic exchange of Ca^{2+} between the SR and the cytosol. These result in the mentioned Ca^{2+} sparks and blinks, the simulation results of which are presented in Figure 7. There is a slight difference in the amplitude of the cytosolic concentration profiles when comparing the Cartesian and curvilinear problems. Similarly, there is not much variation in the sarcoplasmic concentration profiles when comparing the solution on the two different domains. In the Cartesian case, concentration in the SR drops to approximately 580.7–582.5 μM while this drop in the curvilinear case is approximately between 575.9 μM and 585.9 μM (see Figure 7(b) and (d)).

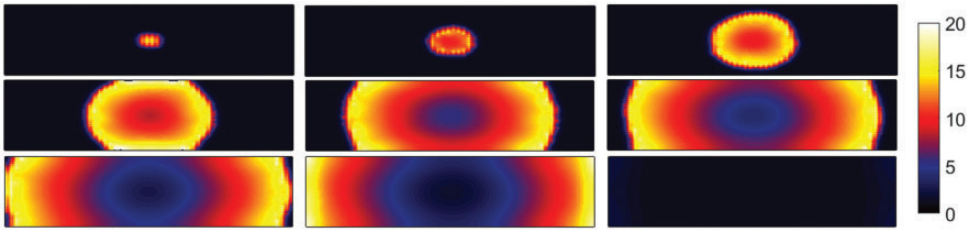

Figure 4. Ca^{2+} wave propagation on the Cartesian grid in the absence of buffer and dye reactions. Snapshots are recorded at times 10, 25, 50, 75, 125, 150, 175, 190 and 300 ms (left to right, top to bottom). The colour bar denotes the Ca^{2+} concentration in μM.

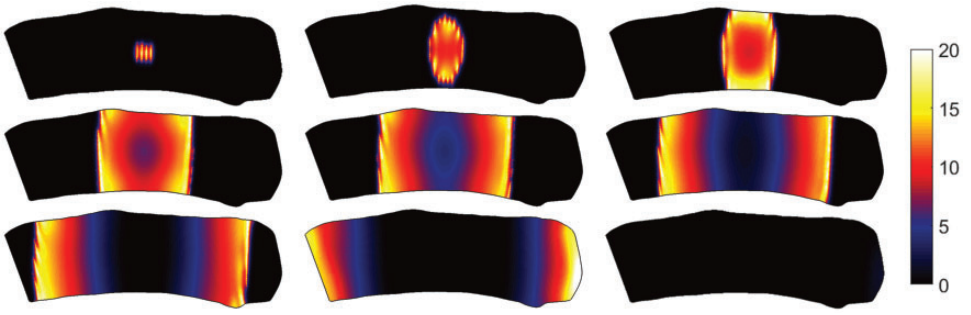

Figure 5. Ca^{2+} wave propagation on the curvilinear grid in the absence of buffer and dye reactions. Snapshots are recorded at times 10, 40, 70, 125, 175, 225, 275, 375 and 550 ms (left to right, top to bottom). The colour bar denotes the Ca^{2+} concentration in μM.

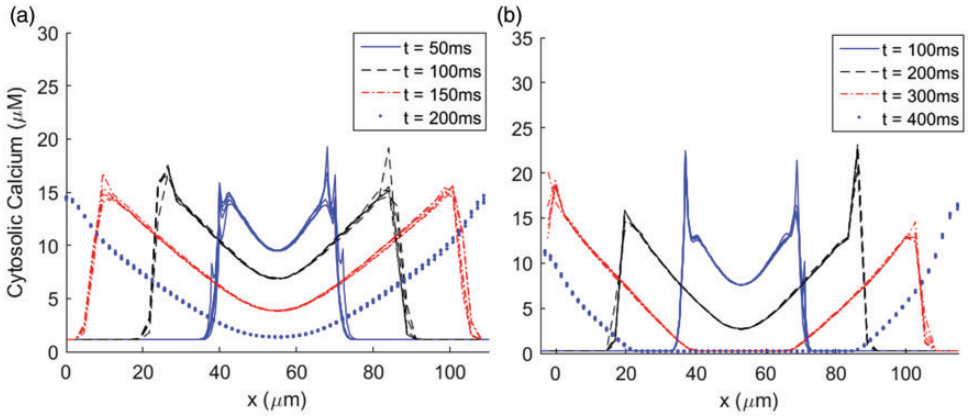

Figure 6. Cytosolic Ca^{2+} wave propagation without buffer and dye reactions. The spatial characteristics of the wave propagation are plotted on the (a) Cartesian domain at times 50, 100, 150 and 200 ms and (b) curvilinear domain at times 100, 200, 300 and 400 ms. Output is given from five separate simulations.

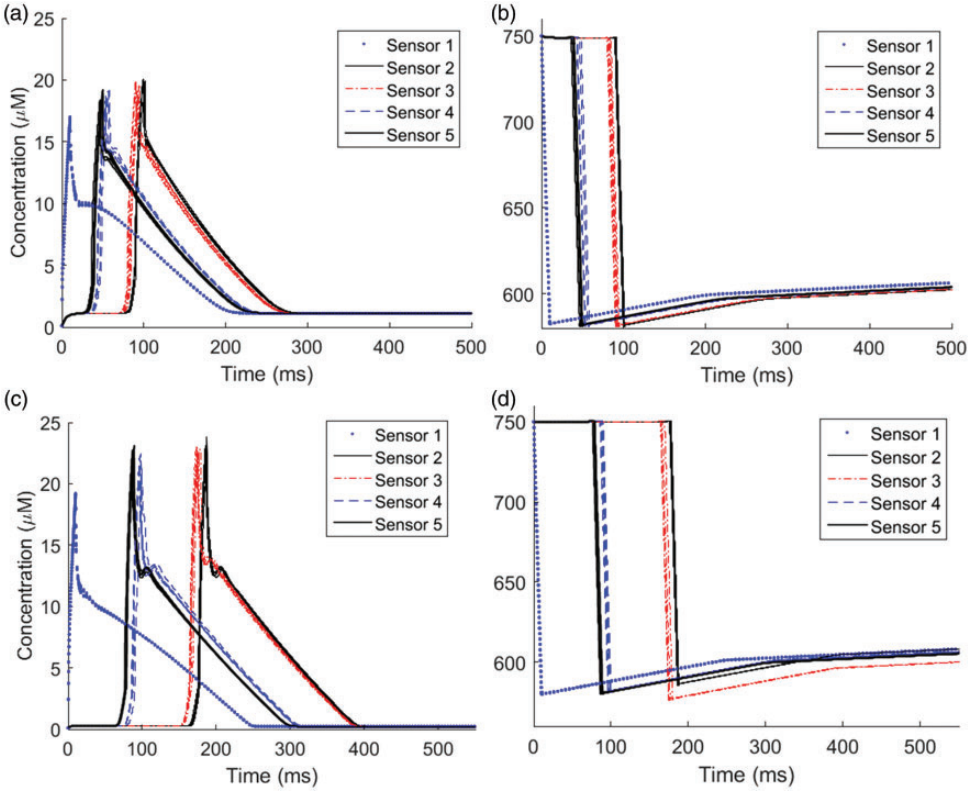

Figure 7. Cytosolic (a, c) and sarcoplasmic (b, d) Ca^{2+} concentrations are plotted on the Cartesian (a, b) and curvilinear (c, d) domains. See Figure 3 in previous section for the location of the sensors. Output is given from five separate simulations.

BD system on the Cartesian and curvilinear domains

In this section, results are presented for the BD system. The same set of equations as in the previous section are solved but with reactions included, i.e. $J_{dye} \neq 0$, $J_{buffer} \neq 0$. Figures 8 and 9 show the Ca^{2+} wave propagation in the presence of buffer and dye reactions. The mean wave velocity is observed to be approximately 167.15 µm/s in the Cartesian and 103.53 µm/s in the curvilinear case. Figure 10 shows the time courses of the wave at times $t =$ 100, 200, 300 and 400 ms (a and c) and the normalised

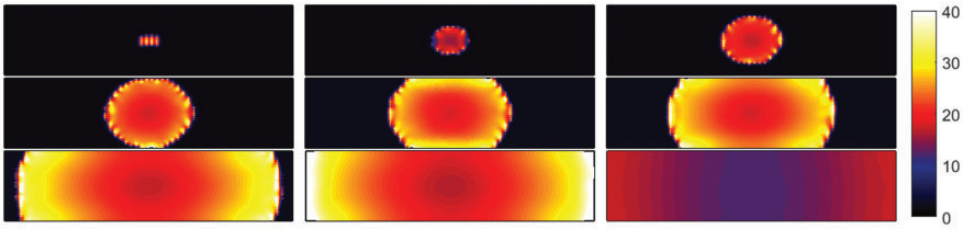

Figure 8. Ca^{2+} wave propagation on the Cartesian grid in the presence of buffer and dye reactions. Snapshots are recorded at times 10, 40, 75, 110, 150, 200, 300, 350 and 700 ms (left to right, top to bottom). The colourbar denotes the Ca^{2+} concentration in μM.

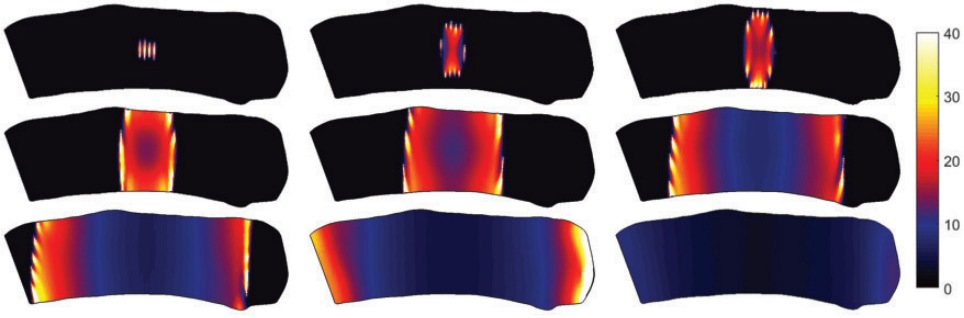

Figure 9. Ca^{2+} wave propagation on the curvilinear grid in the presence of buffer and dye reactions. Snapshots are recorded at times 10, 40, 60, 125, 225, 400, 500, 660 and 900 ms (top to bottom left to right). The colourbar denotes the Ca^{2+} concentration in μM.

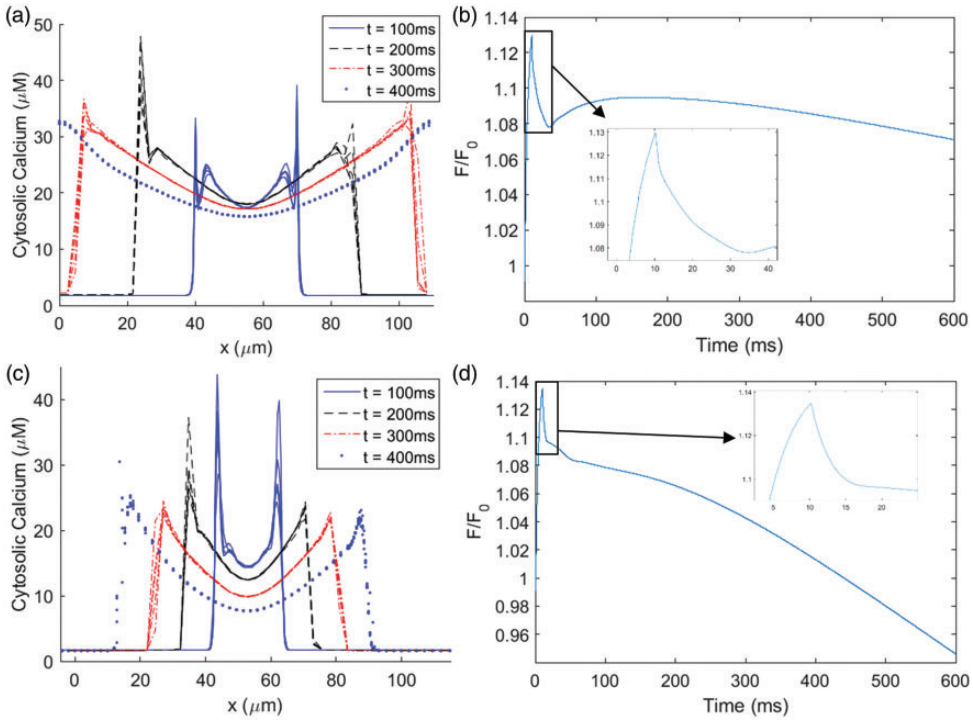

Figure 10. Ca^{2+} wave propagation in the presence of buffer and dye reactions. The spatial characteristics of the wave propagation are plotted at times 100, 200, 300 and 400 ms on the (a) Cartesian and (c) curvilinear domains. Output is given from five separate simulations.

fluorescent indicator dye profile, F/F_0 (b and d). The normalised fluorescent indicator profile is recorded at the cell centre.

The Ca^{2+} concentration increases rapidly initially thus a steep rise in the normalised fluorescent value. The concentration is high enough so that neighbouring sites will activate eventually leading to wave of Ca^{2+}. As Ca^{2+} propagates from the region the concentration will decrease leading to a decrease in the normalised fluorescent values. There is a small delay from initially activated channels to the neighbouring channels becoming active which explains the next two phases in the profile of decreasing then increasing trend. F/F_0 profile peaks at 1.13 and 1.135 in the Cartesian and curvilinear cases, respectively. The shape observed around the peak and the pattern of rise and fall is also observed in experimental[3–6,8,9,17,40–42] and other numerical studies.[17,21,24,26]

A large variation is observed in the sparks and blinks (Figure 11). The amplitude of the sparks range 41.3–53.46 μM with a drop to 71.68–89.62 μM for SR Ca^{2+} content in the Cartesian case (Figure 11(a)) and that in the curvilinear case are 55.67–74.55 μM for spark amplitude and 26.98–80.11 μM for drop in SR Ca^{2+} concentration (Figure 11(c)).

Discussion and conclusion

In this paper, the application of Ca^{2+} waves on curvilinear grids is successfully demonstrated with comparisons against the Cartesian case. This enables the quantitative analysis on Ca^{2+} sparks/blinks and waves by taking into account more realistic cell morphology. The in silico study undertaken here included BD and NBND systems to observe the Ca^{2+} wave characteristics on the different systems. It has been shown in the case of the NBND system that although not much variation was observed in the amplitudes of the cytosolic and sarcoplasmic Ca^{2+} concentration profiles, the computed wave velocity in the Cartesian case was much higher (almost twice as much) than that in the curvilinear case (which is closer to the experimentally observed value of 100 μm/s). After adding buffer and dye, the same parameters become invalid in this new system thus a search for new parameters which produces a meaningful solution is required. In both the BD and NBND cases, the wave velocity calculated on the curvilinear coordinate system provided a closer estimate to that observed experimentally (i.e. 100 μm/s). In the BD cases, the fluorescent indicator dye profiles follow a pattern which is recorded experimentally.

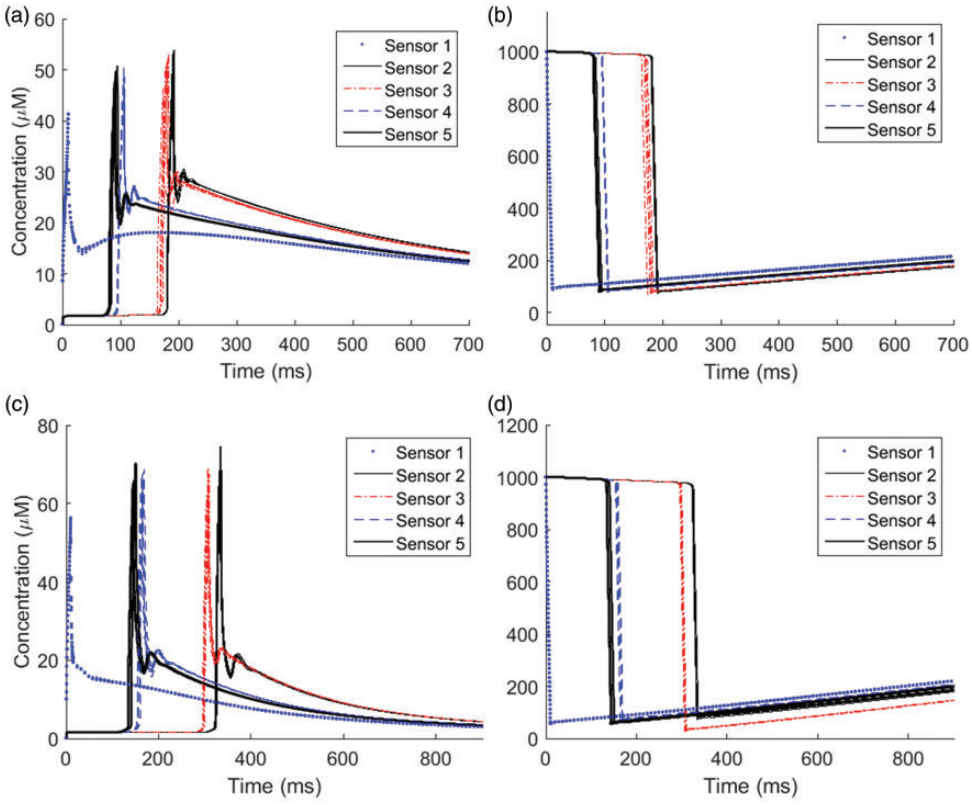

Figure 11. Time courses of the Ca^{2+} wave propagation located at sensors 1–5. Cytosolic Ca^{2+} concentrations are plotted on the (a) Cartesian and (c) curvilinear domains. Similarly, sarcoplasmic Ca^{2+} concentrations are plotted on the (b) Cartesian and (d) curvilinear domains. See Figure 3 in previous section for the location of the sensors. Output is given from five separate simulations.

The variation in spark amplitudes as well as that in SR blinks can be attributed to the fact that the channel sites are dependent on the grid. The same study can be carried out with more information regarding their actual location which can then be applied to both the Cartesian and curvilinear domains.

The formation and development of Ca^{2+} sparks into waves appear differently in the Cartesian and curvilinear grids. The wave propagation region appears to be more elongated in the y-direction for the curvilinear cases. This may be due to either the distribution of CRUs being grid dependent or the partially contracted state of the cell morphology making the distribution of CRUs in the bottom half of the domain more dense and coarser in the top half compared to that in the central part of the cell. In either case, having a curvilinear representation of the problem is a major contribution towards a more realistic cell shape which can handle more sophisticated shapes than the one presented here. The underlying algorithms used in the generation of the curvilinear domain ensure the conformal mapping of grid points. Although some regions will be densely or coarsely populated with grid points the CRDT algorithm maintains a relatively smooth distribution. Therefore, the distribution of CRUs will be dense or coarse in the respective regions accordingly. Having a spatially dependent distribution rather than a grid dependent one will make the curvilinear model more realistic since it is known that CRUs are longitudinally 2 μm and transversely 0.4–0.8 μm apart. The spatial distribution of the channels can be obtained from images of the location of the individual CRUs from experiments. From this, one can directly use this information to set the exact locations on the grid or can derive a spatial distribution function of the channels. The curvilinear domain can easily be adapted to accommodate these points as well as include control functions to have more grid point populated areas possibly around the channels.[43]

A general buffer term was represented by a single ODE. However, it is known that Ca^{2+} can bind to buffers consisting of calmodulin, troponin C, binding sites on the SR and sarcolemmal (SL) membranes. Therefore, a more detailed model accounting for each of these buffers would improve this model. Additionally, Ca^{2+} bound buffers and dye in the SR have different reaction and diffusional properties than that in the cytosol. Therefore, an additional set of equations accounting for this would make this model more comparable to the real case scenario. For the sarcoplasmic Ca^{2+} concentration, an ODE has been used. However, diffusion is also present in this compartment so a PDE can be used to account for this.

Recently, it has been shown that cytosolic Ca^{2+} diffusion follows an anomalous subdiffusion. Fick's Law is known to produce Ca^{2+} full-width at half maximum (FWHM) of 1 μm, half of that observed experimentally. Anomalous subdiffusion is known to address this issue and produce FWHM of closer to 2 μm. Here transformation to curvilinear coordinates is more straightforward with Fick's Law-based diffusion. Bearing this in mind this simplification was maintained in order to demonstrate the application. The model presented in this paper can always be extended to an anomalous subdiffusion model. Although the current work presents a study of stochastic Ca^{2+} sparks and blinks on Cartesian and curvilinear grids it would be interesting to undertake a similar study under deterministic conditions where wave propagation is measured upon a trigger in subcellular release.

Acknowledgements

The authors are greatly thankful to fellow researcher, Christopher Beckwith, for his assistance on generating the orthogonal curvilinear grids and applying the 10th order compact finite difference scheme. The authors would also like to acknowledge the orthogonal grid generator (gridgen-c) provided by Pavel Sakov and CSIRO Marine Research (2006–2017). The code gridgen-c is available at https://github.com/sakov/gridgen-c.

Contributorship

All authors contributed equally to the conception, methodology implementation and manuscript drafting.

Declaration of conflicting interests

The author(s) declared no potential conflicts of interest with respect to the research, authorship, and/or publication of this article.

Funding

The author(s) disclosed receipt of the following financial support for the research, authorship, and/or publication of this article: This work was supported by a Vice-Chancellor's PhD scholarship of the University of Greenwich (reference number: VCS-ACH-15–14).

Ethical approval

None.

Guarantor

SA.

Informed consent

Not applicable.

Trial registration

Not applicable.

ORCID iD

Serife Arif http://orcid.org/0000-0002-6782-3461

References

1. Fabiato A. Calcium-induced release of calcium from the cardiac sarcoplasmic reticulum. *Am J Physiol* 1983; 245: C1–C14.
2. Arif S, Natkunam K, Buyandelger B, et al. An inverse problem approach to identify the internal force of a mechanosensation process in a cardiac myocyte. *Inform Med Unlocked* 2017; 6: 36–42.
3. Cheng H, Lederer WJ and Cannell MB. Calcium sparks: elementary events underlying excitation-contraction coupling in heart muscle. *Science* 1993; 262: 740–744.
4. Cannell MB, Cheng H and Lederer WJ. The control of calcium release in heart muscle. *Science* 1995; 268: 1045–1049.
5. Cheng H, Lederer MR, Lederer WJ, et al. Calcium sparks and [Ca^{2+}]i waves in cardiac myocytes. *Am J Physiol* 1996; 270: C148–C159.
6. Cheng H, Lederer MR, Xiao R-P, et al. Excitation-contraction coupling in heart: new insights from Ca^{2+} sparks. *Cell Calcium* 1996; 20: 129–140.
7. Santana LF, Cheng H, Gomez AM, et al. Relation between the sarcolemmal Ca^{2+} current and Ca^{2+} sparks and local control theories for cardiac excitation-contraction coupling. *Circ Res* 1996; 78: 166–171.
8. Parker I, Zang W-J and Wier WG. Ca^{2+} sparks involving multiple Ca^{2+} release sites along Z-lines in rat heart cells. *J Physiol* 1996; 497: 31–38.
9. Brochet DXP, Yang D, Maio AD, et al. Ca^{2+} blinks: rapid nanoscopic store calcium signalling. *Proc Natl Acad Sci USA* 2005; 102: 3099–3104.
10. Fabiato A. Simulated calcium current can both cause calcium loading in and trigger calcium release from the sarcoplasmic reticulum of a skinned canine cardiac Purkinje cell. *J Gen Physiol* 1985; 85: 291–320.
11. Fabiato A. Time and calcium dependence of activation and inactivation of calcium-induced release of calcium from the sarcoplasmic reticulum of a skinned canine cardiac purkinje cell. *J Gen Physiol* 1985; 85: 247–289.
12. Lopez-Lopez JR, Shacklock PS, Balke CW, et al. Local calcium transients triggered by single l-type calcium channel currents in cardiac cells. *Science* 1995; 268: 1042–1045.
13. Shacklock PS, Wier WG and Balke CW. Local Ca^{2+} transients (Ca^{2+} sparks) originate at the transverse tubules in rat heart cells. *J Physiol (Lond)* 1995; 487: 601–608.
14. Lakatta EG, and and Guarnieri T. Spontaneous myocardial calcium oscillations: are they linked to ventricular fibrillation. *J Cardiovasc Electrophysiol* 1992; 44: 73–89.
15. Lu L, Xia L, Ye X, et al. Simulation of the effect of rogue ryanodine receptors on a calcium wave in ventricular myocytes with heart failure. *Phys Biol* 2010; 7: 026005.
16. Backx PH, Tombe PPD, Deen JHKV, et al. A model of propagating calcium-induced calcium release mediated by calcium diffusion. *J Gen Physiol* 1989; 93: 963–977.
17. Soeller C and Cannell MB. Estimation of the sarcoplasmic reticulum Ca^{2+} release flux underlying Ca^{2+} sparks. *Biophys J* 2002; 82: 2396–2414.
18. Goldbeter A, Dupont G and Berridge MJ. Minimal model for signal-induced Ca^{2+} oscillations and for their frequency encoding through protein phosphorylation. *Proc Natl Acad Sci USA* 1990; 87: 1461–1465.
19. Dupont G and Goldbeter A. Properties of intracellular Ca^{2+} waves generated by a model based on Ca^{2+}-induced Ca^{2+} release. *Biophys J* 1994; 67: 2191–2204.
20. Dupont G and Goldbeter A. Modelling oscillating and waves of cytosolic calcium. *Nonlinear Anal Theory Meth Appl* 1997; 30: 1781–1792.
21. Smith GD, Keizer JE, Stern MD, et al. A simple numerical model of calcium spark formation and detection in cardiac myocytes. *Biophys J* 1998; 75: 15–32.
22. Izu LT, Wier WG and Balke CW. Theoretical analysis of the Ca^{2+} spark amplitude distribution. *Biophys J* 1998; 75: 1144–1162.
23. Izu LT, Mauban JRH, Balke CW, et al. Large currents generate cardiac Ca^{2+} sparks. *Biophys J* 2001; 80: 88–102.
24. Tan W, Fu C, Xie W, et al. An anomalous subdiffusion model for calcium spark in cardiac myocytes. *Appl Phys Lett* 2007; 91: 183901.
25. Tracqui P and Ohayon J. An integrated formulation of anisotropic force-calcium relations driving spatio-temporal contractions of cardiac myocytes. *Phil Trans R Soc A* 2009; 367: 4887–4905.
26. Li K, Fu C, Cheng H, et al. Anomalous subdiffusion of calcium spark in cardiac myocytes. *Cel Mol Bioeng* 2011; 4: 457–465.
27. Izu LT, Wier WG and Balke CW. Evolution of cardiac calcium waves from stochastic calcium sparks. *Biophys J* 2001; 80: 103–120.
28. Chen X, Kang J, Fu C, et al. Modelling calcium wave based on anomalous subdiffusion of calcium sparks in cardiac myocytes. *PLoS ONE* 2013; 8: e57093.
29. Chen X, Guo L, Kang J, et al. Calcium waves initiating from the anomalous subdiffusive calcium sparks. *J R Soc* 2014; 11: 20130934.
30. Li J, Xie W, Chen X, et al. A novel stochastic reaction–diffusion model of Ca^{2+} blink in cardiac myocytes. *Sci Bull* 2017; 62: 5–8.
31. Subramanian S, Viatchenko-Karpinski S, Lukyanenko V, et al. Underlying mechanisms of symmetric calcium wave propagation in rat ventricular myocytes. *Biophys J* 2001; 80: 1–11.
32. Ruiz-Baier R, Gizzi A, Rossi S, et al. Mathematical modelling of active contraction in isolated cardiomyocytes. *Math Med Biol* 2014; 31: 259–283.
33. Dupont G and Goldbeter A. Oscillations and waves of cytosolic calcium: insights from theoretical models. *BioEssays* 1992; 14: 485–493.
34. Engel J, Fechner M, Sowerby AJ, et al. Anisotropic propagation of Ca^{2+} waves in isolated cardiomyocytes. *Biophys J* 1994; 66: 1756–1762.
35. Arif S, Lai C-H and Nadarajah R. Modelling stochastic calcium waves in cardiac myocytes based on the two-pool CICR model. *Comput Cardiol* 2017; 44: 1-4.

36. Press WH, Teukolsky SA, Vetterling WT, et al. *Numerical recipes: the art of scientific computing*. 3rd ed. New York: Cambridge University Press, 2007.
37. Driscoll TA and Vavasis SA. Numerical conformal mapping using cross-ratios and Delaunay triangulation. *SIAM J Sci Comput* 1998; 19: 1783–1803.
38. Lele SK. Compact finite difference schemes with spectral-like resolution. *J Comput Phys* 1992; 103: 16–42.
39. Takamatsu T and Wier WG. Calcium waves in mammalian heart: quantification of origin, magnitude, waveform, and velocity. *FASEB J* 1990; 4: 1519–1525.
40. Cheng H and Lederer WJ. Calcium sparks. *Physiol Rev* 2008; 88: 1491–1545.
41. Fearnley CJ, Roderick HL and Bootman MD. Calcium signalling in cardiac myocytes. *Cold Spring Harb Perspect Biol* 2011; 3: a004242.
42. Bers DM and Shannon TR. Calcium movements inside the sarcoplasmic reticulum of cardiac myocytes. *J Mol Cell Cardiol* 2013; 58: 59–66.
43. Hoffmann KA and Chiang ST. *Computational fluid dynamics Volume I. 4th ed. Engineering Education System*. Washington, DC, USA, 2000.

Appendix 1

The numerical conversion for the source strength, K_s, involves the Green's function obtained from the analytical solution of the diffusion problem for the two-dimensional case and convolving this with the Heaviside function. Some description on the derivation is given previously.[27] The deduced relations for each of the Cartesian and curvilinear cases are given below. For an anisotropic case where $D_{Cx} = 0.3\ \mu m^2/ms$ and $D_{Cy} = D_{Cz} = 0.15\ \mu m^2/ms$, the following is obtained for the molar flux, σ, that contains the source strength

$$\sigma = \frac{7.74596669\left(1 - \operatorname{erf}\left(\left\{\frac{0.05270462768}{\sqrt{30\left(\Delta x^2 + 2(\Delta y^2 + \Delta z^2)\right)}}\right\}\right)\right)}{\sqrt{30\left(x^2 + 2(y^2 + z^2)\right)}\,E_1\left(\left\{\begin{array}{c}0.08333333333\Delta x^2 \\ +\,0.1666666667\Delta y^2\end{array}\right\}\right)}\sigma_3 \tag{7}$$

where $E_1(x) = \int_z^\infty \frac{e^{-t}}{t}\mathrm{d}t$ is an exponential integral. Δx, Δy and Δz are distances between points in the x, y and z directions, respectively. In the case of the Cartesian coordinates, the molar flux is a scalar. However, in curvilinear coordinates, it is spatially dependent and becomes a vector.